Electronic Supplementary Material (ESI) for Journal of Materials Chemistry A.

Supporting Information:

Supramolecular reinforcement drastically enhances thermal conductivity of interpenetrated covalent organic frameworks

Sandip Thakur* and Ashutosh Giri*

Department of Mechanical, Industrial and Systems Engineering, University of Rhode Island,
Kingston, RI 02881, USA

E-mail: sandip_thakur@uri.edu; ashgiri@uri.edu

Table (S1) Elastic moduli (E) and thermal conductivities (κ) of different materials at room temperature.

Material	E (GPa)	Refs.	κ (W m^{-1} K^{-1})	Refs.
Ge	135.4	Ref. S1	60.2	Ref. S2
Si	165.82	Ref. S1	149	Ref. S2
Diamond (I)	1144.81	Ref. S1	900	Ref. S2
Diamond (IIa)	1144.81	Ref. S1	2320	Ref. S2
Diamond (IIb)	1144.81	Ref. S1	1360	Ref. S2
SnTe	65.36	Ref. S3	8.2	Ref. S4
PbTe	67.23	Ref. S3	1.7	Ref. S5
SnTe:Ga, x=0.1	68.3	Ref. S3	6.3	Ref. S4
InAs	79.7	Ref. S6	27	Ref. S7
$SrTiO_3$	260.85	Ref. S8	11	Ref. S9
Ag_8SnSe_6	52.63	Ref. S10	0.39	Ref. S10
MgO	310	Ref. S11	52	Ref. S12
J30	236.7	Ref. S12	1.68	Ref. S12
Al_2O_3	345	Ref. S12	34	Ref. S12
$MAPbI_3$	12	Ref. S13	0.35	Ref. S13
$CsPbbr_3$	13.5	Ref. S13	0.46	Ref. S13
$MAPbBr_3$	17.8	Ref. S13	0.51	Ref. S13
$MAPbCl_3$	23	Ref. S13	0.73	Ref. S13
YB_66	362.69	Ref. S14	2.55	Ref. S15
$(Co_6Te_8)(C_{60})_2$	1.5	Ref. S16	0.16	Ref. S16
Co_6Se_8	2.3	Ref. S16	0.18	Ref. S16
$(Co_6Se_8)(C_{60})_2$	8.1	Ref. S16	0.25	Ref. S16
Co_6S_8	4	Ref. S16	0.22	Ref. S16
C_60	10	Ref. S17	0.4	Ref. S18
$La_2Zr_2O_7$	175	Ref. S19	1.9	Ref. S19
$BaZrO_3$	181	Ref. S19	4.3	Ref. S19
NiO	175	Ref. S20	34	Ref. S21
B_9C	350	Ref. S22	3.9	Ref. S23
Kevlar	185	Ref. S24	3.1	Ref. S25
Zylon	275	Ref. S25	23	Ref. S25
Nomex	88	Ref. S26	0.65	Ref. S27
Polyamides	9.98	Ref. S28	0.4	Ref. S28
Vinyls	5.96	Ref. S28	0.2	Ref. S28
Polyesters	15.05	Ref. S28	0.2	Ref. S28
Polyethylene (PE)	18.08	Ref. S28	0.4	Ref. S28
MOF-5	17.59	Ref. S29	0.34	Ref. S30
COF-5	11.53	Ref. S31	1	Ref. S32

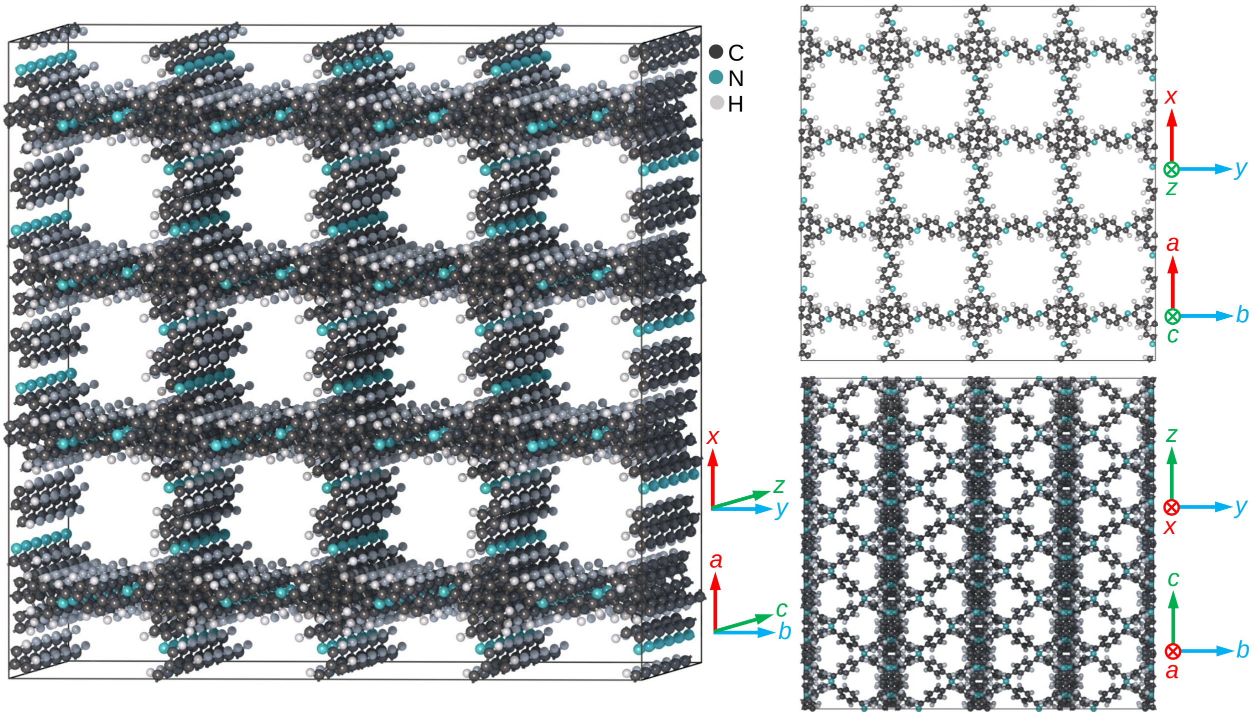

Figure (S1) Schematic illustration of the computational domain for our pristine COF-300 structure highlighting the directional variation along the in-plane (a- and b-) and cross-plane (c-) directions.

I. Equilibrium MD (EMD) Simulations

We utilize the Green-Kubo (GK) formalism under the equilibrium molecular dynamics (EMD) simulations framework to predict the thermal conductivity of our COF-300 structures using the LAMMPS package.[S33] In this method, the thermal conductivity is calculated as,

$$\kappa_\alpha = \frac{1}{k_\mathrm{B} V T^2} \int_0^\infty \langle J_\alpha(t) J_\alpha(0) \rangle dt. \tag{1}$$

Here, t is the time, T and V are the temperature and volume of the system, and $\langle J_\alpha(t) J_\alpha(0) \rangle$ is the αth component of the heat current autocorrelation function (HCACF) which is given as,[S34]

$$\mathrm{J} = \frac{1}{V} \left(\sum_i v_i \epsilon_i + \sum_i \mathrm{S}_i \cdot v_i \right). \tag{2}$$

Here, v_i, ϵ_i, and S_i represent the velocity, energy and stress of atom i, respectively.

For our equilibration process, the structures are initially equilibrated under the Nosé-Hoover thermostat and barostat (i.e. the NPT ensemble)[S35] for 1 ns with a timestep of 0.5 fs where the number of particles, pressure and temperature of the system are held constant at 0 bar pressure. Following the NPT integration, further equilibration is carried out under the NVT ensemble where the volume and temperature are kept constant for a total of 1 ns with periodic boundary conditions in all three directions for the entire simulation. An additional equilibration is performed under NVE ensemble for 1 ns where the number of particles, volume and total energy of the system are held constant. Finally, we utilize the GK formalism to calculate the thermal conductivities of the computational domains.

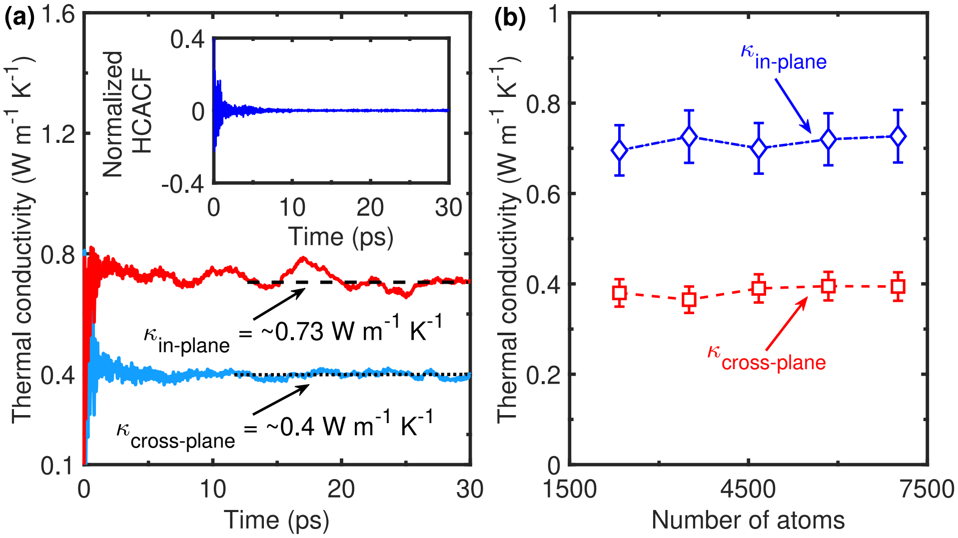

Figure (S2) (a) Green-Kubo thermal conductivity of our pristine COF-300 structure at 300 K as a function of the integration time. Normalized heat current autocorrelation function (HCACF) as a function of the integration time is shown in the inset. The converged thermal conductivity is determined by averaging from 10 to 30 ps where the HCACF has fully decayed to zero. (b) Thermal conductivity of pristine COF-300 structure in in-plane and cross-plane directions at 300 K as a function of number of atoms in the computational domains. Note, we consider the computational domain of our pristine COF-300 structure with 7008 atoms to calculate the thermal conductivities across the temperature range.

We use the total correlation time period of 30 ps for the integration of the HCACF as shown in the inset of Fig. S2a. The heat current is calculated every 7 fs for all temperatures during the data collection period followed by integration of the heat current to calculate the converged thermal conductivities. We note that our choice of sampling rate for the HCACF has negligible influence on the predicted thermal conductivities. Figure S2a shows the converged in-plane and cross-plane thermal conductivities for the pristine COF-300 structure at 300 K, which is determined by integrating from 10 ps to 30 ps where the HCACF has fully decayed to zero as shown in the inset. Note, we calculate the in-plane thermal conductivity by taking average of thermal conductivities in x- and y-directions ($\kappa_{\text{in-plane}} = \frac{1}{2}[\kappa_x + \kappa_y]$). To ensure our results are not influenced by the size of our computational domains, we carried out a series of GK calculations by varying the size of the computational domain (and the number of atoms from 2336 to 7008) as shown in Fig. S2b. The convergence of thermal conductivity for the different computational domain sizes within uncertainties ensures that our choice of the domain size with 7008 atoms does not influence our GK predictions. To gain confidence in our GK-predictions, we also perform additional non-equilibrium molecular dynamics (NEMD) simulations to calculate the room temperature thermal conductivity as shown in Fig. S3. Note, since the NEMD method is computationally very expensive (especially with the costly ReaxFF potential) with large domain sizes, we only perform a set of NEMD simulations to calculate the cross-plane thermal conductivity of our COF-300 structure.

We have used this method previously to study the influence of guest-host interactions in 2D COFs.[S36,S37] Our recent computational investigations have revealed that the thermal conductivity of 2D COFs is significantly affected by infiltration of guest molecules.[S36,S37] These works have shown that the comprehensive understanding of the impact of guest molecules on thermal conductivity is complex due to factors such as additional scattering at pore walls that might reduce phonon thermal conductivity,[S37] influence of varying pore geometries that might increase or decrease thermal conductivity depending on the node and the linkers,[S38] density variations in the guest infiltration that can vary thermal conductivity over a wide range,[S37] and additional heat transfer channels that might increase the overall thermal conductivity of gas-loaded COFs.[S36] For example, in smaller-pore 2D COFs such as COF-1, guest molecules reduce thermal conductivity due to solid-gas scattering, while larger-pore COFs (such as COF-5, TP-COF) with infiltrated guest molecules exhibit increased cross-plane thermal conductivity due to additional heat conduction channels introduced from the confined gas molecules.[S37] As guest infiltration can either increase or decrease the thermal conductivity, fully understanding the consequences of such infiltrations in COF-300 requires further investigation but falls beyond the scope of the current work.

Furthermore, a high degree of conjugation can result in a significant enhancement in thermal transport, as evidenced by previous studies.[S39–S41] This effect has been observed in various materials such as in two-dimensional crystalline polymersS[S40,S42] with extensive π-conjugation and high bond energy in their molecular backbones exhibit notably high thermal conductivity. Therefore, the extended conjugation in COFs might also impact the phonon dynamics, resulting in variations in their thermal conductivity. In our study, segregating the contributions arising from π-conjugation in our COF-300 structures requires a detailed investigation and therefore deserves further investigation.

II. Non-equilibrium MD (NEMD) Simulations

To further support our results obtained from the GK formalism under the EMD simulations framework, we perform additional NEMD simulations using the LAMMPS package[S33] and validate the thermal conductivity of our pristine COF-300 structure in the cross-plane, z-direction. In this technique, we establish a steady-state temperature profile across our computational domain by imposing a heat flux. This is carried out by prescribing a 'hot' region located at one end of the computational domain, where we add energy at a constant rate and simultaneously extract the equal amount of energy from the 'cold' region located at the other end of the computational domain. We divide our computational domain into distinct regions along the z-direction, as illustrated in Fig. S3a. The atoms within the 'wall' region are frozen, while a fixed amount of heat is added and removed from the atoms within the 'hot bath' and 'cold bath' regions, respectively.

After we obtained a steady-state temperature profile as shown in Fig. S3b, the thermal conductivity is calculated by invoking the Fourier's law of heat conduction,

$$Q = -\kappa \frac{dT}{dx}. \tag{3}$$

Here, Q represents the heat flux that is added to and subtracted from the hot and cold regions, respectively. κ denotes the thermal conductivity, while $\frac{dT}{dx}$ represents the steady-state temperature gradient.

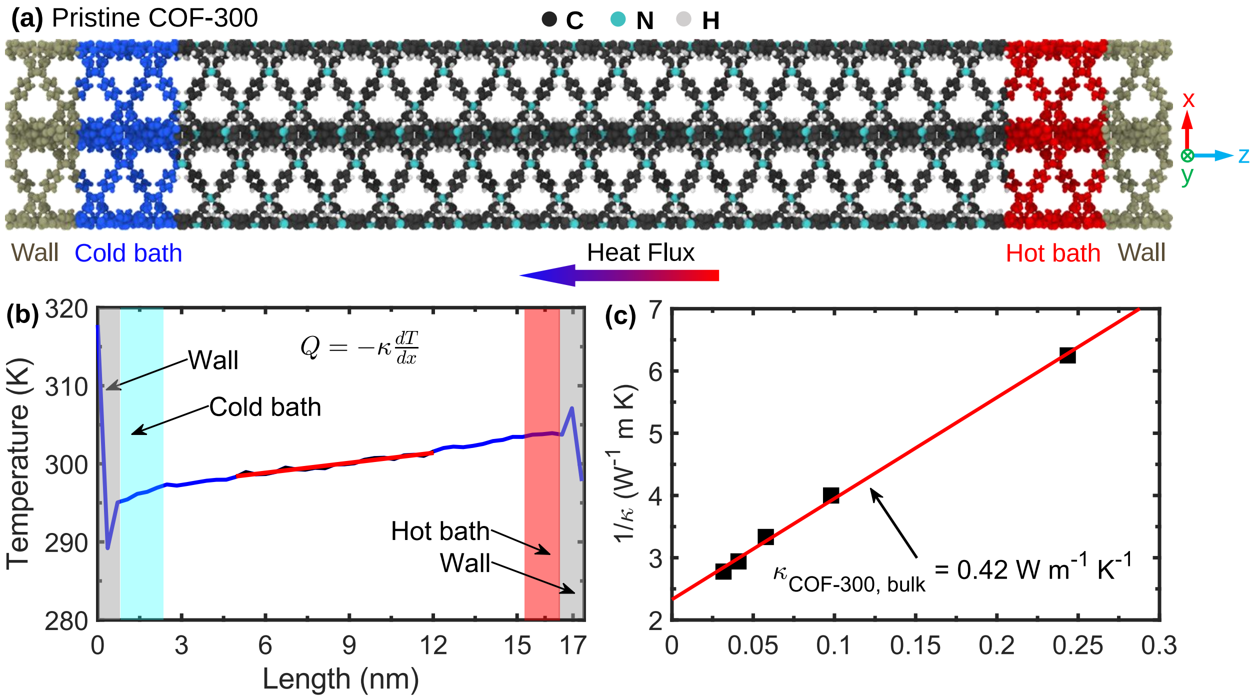

Figure (S3) (a) Schematic illustration of the computational domain for our pristine COF-300 structure used in our NEMD simulations to predict the cross-plane thermal conductivity. (b) Characteristic steady-state temperature profile in the z-direction, which we utilize to calculate the thermal conductivity by invoking the Fourier's law of heat conduction. (c) NEMD-predicted inverse of size-dependent thermal conductivities as a function of the inverse of the computational domain length in the applied heat flux direction. The 'bulk' thermal conductivity is predicted by extrapolating the linear fit to $1/L \rightarrow 0$.[S43,S44]

Figure S3 shows the details of the NEMD simulations performed on our pristine COF-300 structure in the cross-plane direction. We calculated the thermal conductivity for different computational domain lengths ranging from 70 to 360 Å. Initially, the computational domain of our pristine COF-300 structure is equilibrated under the Nosé Hoover thermostat and barostat[S35] using the NPT integration for a total of 1 ns where the number of particles, pressure and temperature of the system are held constant at 0 bar pressure using a timestep of 0.5 fs. Then the structure is further equilibrated under an NVT integration where the volume and temperature is kept constant for a total of 1 ns with periodic boundary conditions in all three directions for the entire simulation.

Further, an additional equilibration is performed under NVE ensemble for 1 ns where the number of particles, volume and total energy of the system are maintained constant. Finally, we utilize the NEMD method as mentioned above to calculate the thermal conductivity of our pristine COF-300 domains. As carried out in prior works,[S43,S44] we plot the inverse of thermal conductivity versus the inverse of the computational domain length (L) and extrapolate to $L \to 0$ to obtain the bulk thermal conductivity as shown in Fig. S3c. We calculate a $\kappa_{\mathrm{cross-plane}}$ = 0.42±0.06 W m^{-1} K^{-1} via our NEMD approach which agrees very well with 0.4±0.05 W m^{-1} K^{-1} calculated by our GK method, thus providing confidence in the results presented in this work.

III. Vibrational Density of States

To determine the vibrational density of states (DOS) for our COF-300 structures, we recorded the velocities of the atoms at intervals of 10 time steps over a duration of 1 nanosecond. Once we gathered the time series data for velocity fluctuations, we employed the Fourier transformation algorithm on the velocity autocorrelation function (VACF). Additionally, we utilized the Welch method of power spectral density estimation to obtain the DOS.

$$D(\omega) = \frac{1}{2k_{\mathrm{B}}T} m(\mathrm{VACF})\rho. \tag{4}$$

Here m is the atomic mass. T, k_{B}, and ρ are the local temperature, Boltzmann constant, and atomic density, respectively.

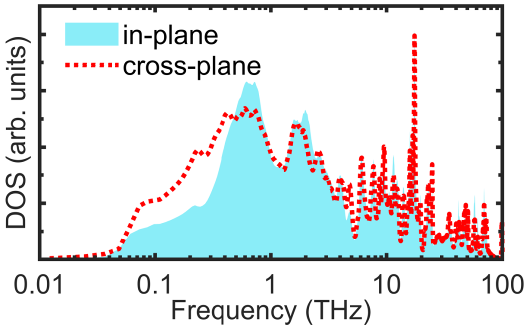

Figure (S4) Vibrational density of states of pristine structure in the in-plane and cross-plane directions. There is higher vibrational DOS of the lower frequency modes in the cross-plane direction. The shift to higher frequency vibrations in the in-plane direction might be one of the reasons for the enhanced thermal conductivity in that direction (as shown in Fig. 2b).

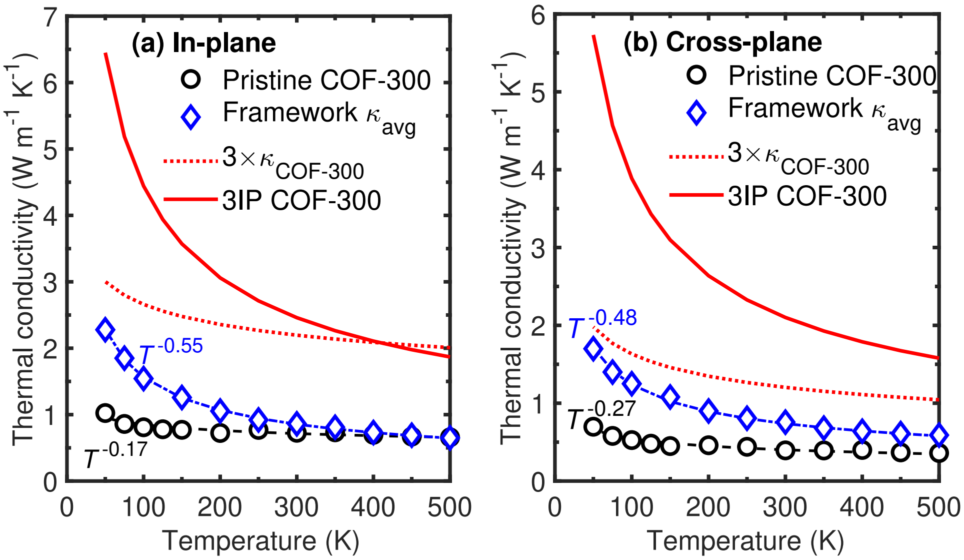

Figure (S5) Calculated thermal conductivities as a function of temperature for the pristine COF-300 compared to the thermal conductivity contributions from the individual frameworks of 3IP COF-300 structure in the (a) in-plane and (b) cross-plane directions. Thermal conductivities of the sum of 3 frameworks (signifying parallel channels of heat transfer without the influence of supramolecular interactions) and 3IP COF-300 structure (with the influence of supramolecular interactions) are also included for comparison. As is clear, supramolecular interactions in the interpenetrated frameworks result in considerably higher thermal conductivities as compared to the 3× thermal conductivities (especially at lower temperatures and along the in-plane direction). This highlights the significant increment in thermal transport via supramolecular interactions that significantly change the thermal conductivities of the individual frameworks in the interpenetrated structures.

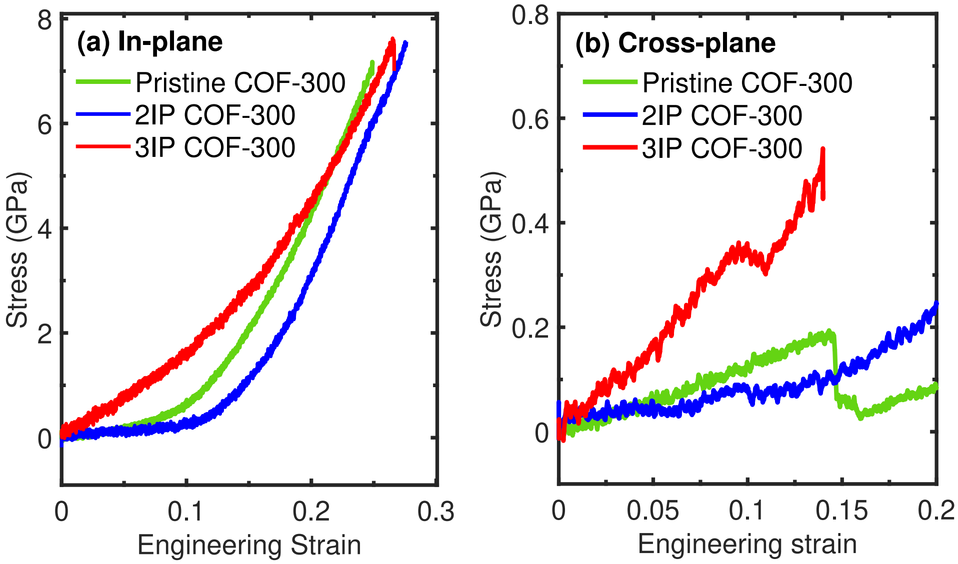

Figure (S6) Stress versus strain curves for uniaxial tensile loading in the (a) in-plane (x-direction) and (b) cross-plane directions (z-direction) for our pristine, 2IP, and 3IP COF-300 structures.

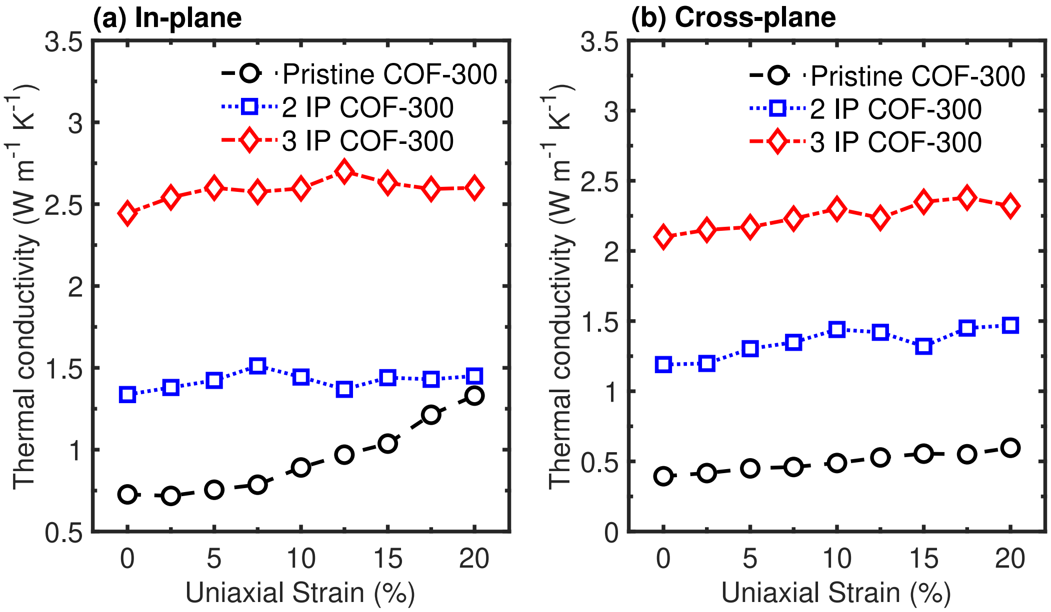

Figure (S7) Thermal conductivities as a function of uniaxial tension for our pristine, 2IP, and 3IP COF-300 structures in the (a) in-plane and (b) cross-plane directions. We note that the structures are stretched in the in-plane (x-) and cross-plane (z-) directions to calculate their thermal conductivities in the respective directions. The thermal conductivity increases monotonically with increase in uniaxial strain for our pristine COF-300 structure in both the in-plane and cross-plane directions. However, the effect of strain on the thermal conductivities for 2IP and 3IP structures has a reduced effect in both the in-plane and cross-plane directions.

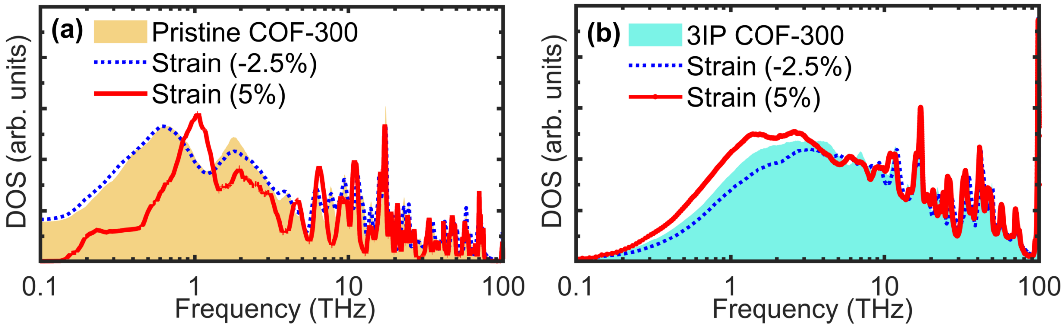

Figure (S8) Vibrational density of states of our (a) pristine and (b) 3IP COF-300 structures at 300 K for 5% hydrostatic tension and 2.5% hydrostatic compression. We see considerable shift in the vibrational spectrum to higher frequencies for pristine COF-300 structure resulting in the phonon hardening and higher thermal conductivities under hydrostatic tension (a). Whereas, for the 3IP COF-300 structure (b), due to reduced supramolecular interactions between the COF frameworks, vibrational spectrum considerably shifts to lower frequencies resulting in the lower thermal conductivities for the interpenetrated structures as compared to the pristine COF-300 (as shown in Fig. 5 of the main text.

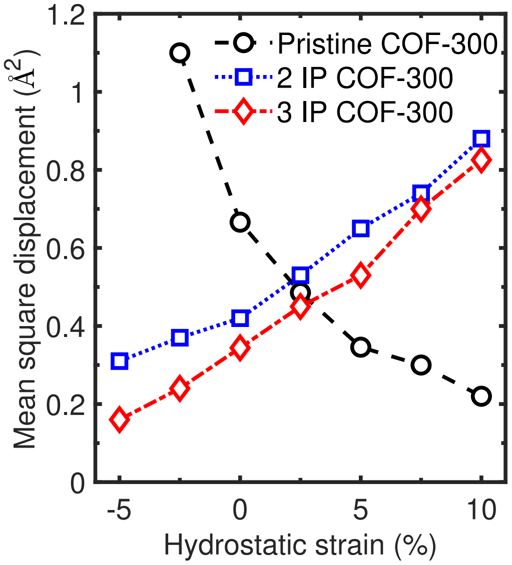

Figure (S9) Calculated mean square displacements (MSDs) of our pristine and interpenetrated COF-300 structures at 300 K as a function of hydrostatic strain. The MSDs for pristine COF-300 structure are reduced due to better alignment of the polymer chains (see Fig. S11) resulting in the phonon hardening and higher thermal conductivities under hydrostatic tension. Whereas, for the interpenetrated COF-300 structures, due to reduced supramolecular interactions between the COF frameworks, the MSDs are increased with the application of hydrostatic tensile strains resulting in the lower thermal conductivities for the interpenetrated structures as compared to the pristine COF-300 (as shown in Fig. 5 of the main text.)

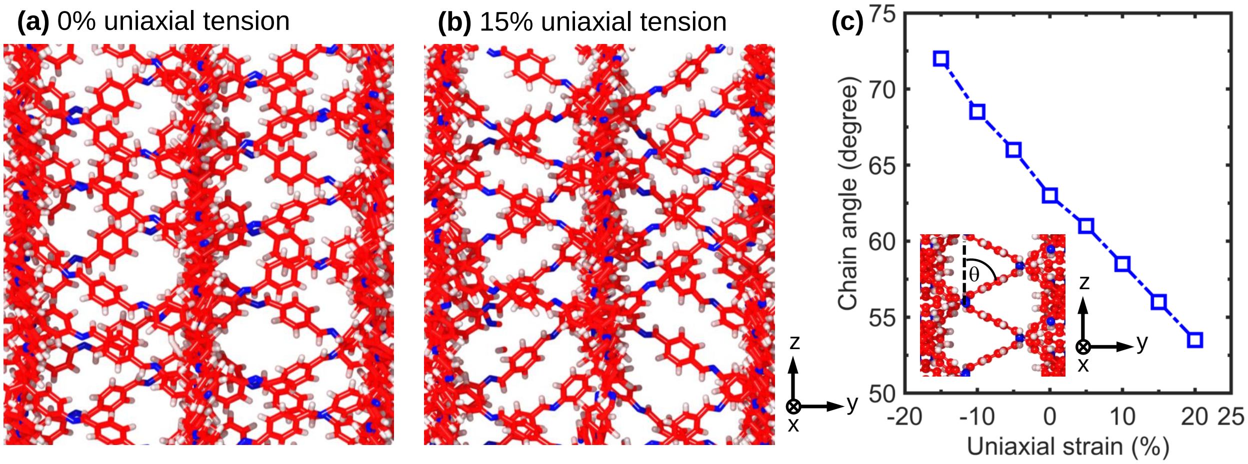

Figure (S10) Schematics of our pristine COF-300 structure for (a) 0% and (b) 10% uniaxial tensions in z-direction. (c) Chain angle between the polymeric linkers and the cross-plane axis as a function of uniaxial strain for our pristine COF-300 structure at room temperature. We observe monotonic decrease in the chain angle with the increase in uniaxial strain. This decrease in chain angle leads to better alignment of the polymeric chain linkers along the cross-plane direction and thus facilitate heat transfer along that direction (Fig. 2c).

(a) 0% hydrostatic tension

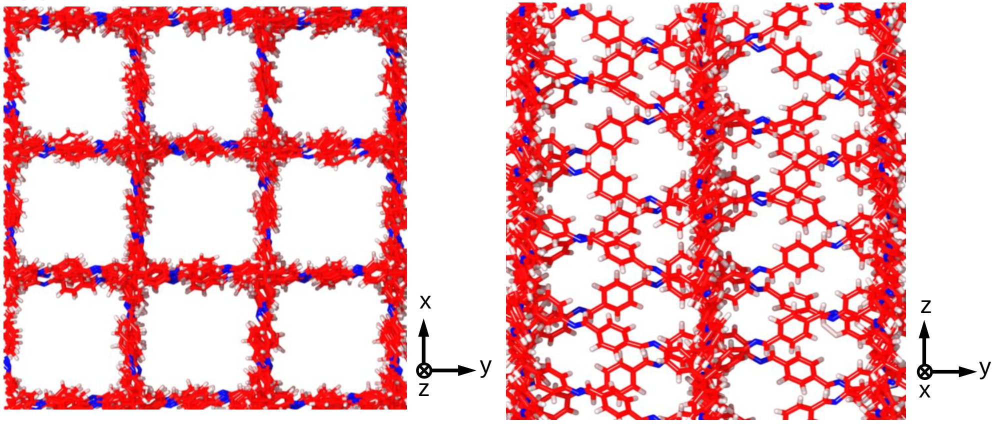

(b) 10% hydrostatic tension

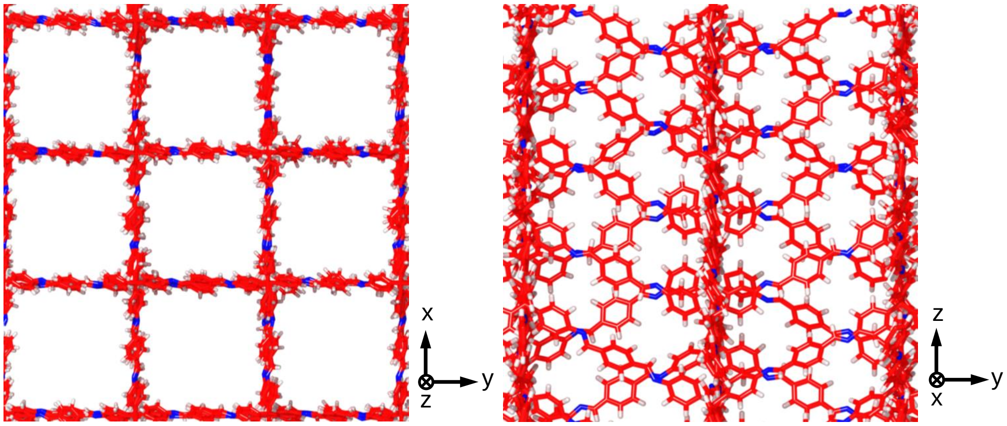

Figure (S11) Schematics of our pristine COF-300 structure for (a) 0% and (b) 10% hydrostatic tensions. Hydrostatic tension results in better alignment of the polymer chains leading to vibrational hardening and the concomitant increase in the thermal conductivity of the pristine COF-300 structure (Figs. 5b and 5c).

References

(S1) American Institute of Physics,; Gray, D. E. *American Institute of Physics Handbook: 3d Ed*; McGraw-Hill, 1972.

(S2) Ho, C. Y.; Powell, R. W.; Liley, P. E. Thermal conductivity of the elements. *Journal of Physical and Chemical Reference Data* **1972**, *1*, 279–421.

(S3) Miller, A.; Saunders, G.; Yogurtcu, Y. Pressure dependences of the elastic constants of PbTe, SnTe and Ge0. 08Sn0. 92Te. *Journal of Physics C: Solid State Physics* **1981**, *14*, 1569.

(S4) Al Rahal Al Orabi, R.; Hwang, J.; Lin, C.-C.; Gautier, R.; Fontaine, B.; Kim, W.; Rhyee, J.-S.; Wee, D.; Fornari, M. Ultralow lattice thermal conductivity and enhanced thermoelectric performance in SnTe: Ga materials. *Chemistry of Materials* **2017**, *29*, 612–620.

(S5) Morelli, D.; Jovovic, V.; Heremans, J. Intrinsically minimal thermal conductivity in cubic I-V- VI 2 semiconductors. *Physical Review Letters* **2008**, *101*, 035901.

(S6) Gerlich, D. Elastic constants of single-crystal indium arsenide. *Journal of Applied Physics* **1963**, *34*, 2915–2915.

(S7) Maycock, P. Thermal conductivity of silicon, germanium, III–V compounds and III–V alloys. *Solid-State Electronics* **1967**, *10*, 161–168.

(S8) Bell, R.; Rupprecht, G. Elastic constants of strontium titanate. *Physical Review* **1963**, *129*, 90.

(S9) Oh, D.-W.; Ravichandran, J.; Liang, C.-W.; Siemons, W.; Jalan, B.; Brooks, C. M.; Huijben, M.; Schlom, D. G.; Stemmer, S.; Martin, L. W., et al. Thermal conductivity as a metric for the crystalline quality of SrTiO 3 epitaxial layers. *Applied Physics Letters* **2011**, *98*, 221904.

(S10) Li, L.; Liu, Y.; Dai, J.; Hong, A.; Zeng, M.; Yan, Z.; Xu, J.; Zhang, D.; Shan, D.; Liu, S., et al. High thermoelectric performance of superionic argyrodite compound Ag 8 SnSe 6. *Journal of Materials Chemistry C* **2016**, *4*, 5806–5813.

(S11) Chung, D.-H. Elastic moduli of single crystal and polycrystalline MgO. *Philosophical Magazine* **1963**, *8*, 833–841.

(S12) Braun, J. L.; Rost, C. M.; Lim, M.; Giri, A.; Olson, D. H.; Kotsonis, G. N.; Stan, G.; Brenner, D. W.; Maria, J.-P.; Hopkins, P. E. Charge-induced disorder controls the thermal conductivity of entropy-stabilized oxides. *Advanced Materials* **2018**, *30*, 1805004.

(S13) Elbaz, G. A.; Ong, W.-L.; Doud, E. A.; Kim, P.; Paley, D. W.; Roy, X.; Malen, J. A. Phonon speed, not scattering, differentiates thermal transport in lead halide perovskites. *Nano Letters* **2017**, *17*, 5734–5739.

(S14) Slack, G. A.; Oliver, D. W.; Brower, G.; Young, J. Properties of melt-grown single crystals of “YB68”. *Journal of Physics and Chemistry of Solids* **1977**, *38*, 45–49.

(S15) Cahill, D. G.; Watson, S. K.; Pohl, R. O. Lower limit to the thermal conductivity of disordered crystals. *Physical Review B* **1992**, *46*, 6131.

(S16) Ong, W.-L.; O’Brien, E. S.; Dougherty, P. S.; Paley, D. W.; Fred Higgs III, C.; McGaughey, A. J.; Malen, J. A.; Roy, X. Orientational order controls crystalline and amorphous thermal transport in superatomic crystals. *Nature Materials* **2017**, *16*, 83–88.

(S17) Kolomenskii, A. A.; Szabadi, M.; Hess, P. Laser diagnostics of C60 and C70 films by broadband surface acoustic wave spectroscopy. *Applied Surface Science* **1995**, *86*, 591–596.

(S18) Tea, N.; Yu, R. C.; Salamon, M.; Lorents, D.; Malhotra, R.; Ruoff, R. Thermal conductivity of C 60 and C 70 crystals. *Applied Physics A* **1993**, *56*, 219–225.

(S19) Vassen, R.; Cao, X.; Tietz, F.; Basu, D.; Stöver, D. Zirconates as new materials for thermal barrier coatings. *Journal of the American Ceramic Society* **2000**, *83*, 2023–2028.

(S20) Jifang, W.; Fisher, E.; Manghnzmi, M. Elastic constants of nickel oxide. *Chinese Physics Letters* **1991**, *8*, 153.

(S21) Lewis, F.; Saunders, N. The thermal conductivity of NiO and CoO at the Neel temperature. *Journal of Physics C: Solid State Physics* **1973**, *6*, 2525.

(S22) Thevenot, F. Boron carbide—a comprehensive review. *Journal of the European Ceramic society* **1990**, *6*, 205–225.

(S23) Beekman, M.; Cahill, D. G. Inorganic crystals with glass-like and ultralow thermal conductivities. *Crystal Research and Technology* **2017**, *52*, 1700114.

(S24) Chae, H. G.; Kumar, S. Rigid-rod polymeric fibers. *Journal of Applied Polymer Science* **2006**, *100*, 791–802.

(S25) Wang, X.; Ho, V.; Segalman, R. A.; Cahill, D. G. Thermal conductivity of high-modulus polymer fibers. *Macromolecules* **2013**, *46*, 4937–4943.

(S26) Tashiro, K.; Kobayashi, M.; Tadokoro, H. Elastic moduli and molecular structures of several crystalline polymers, including aromatic polyamides. *Macromolecules* **1977**, *10*, 413–420.

(S27) Kawabata, S.; Rengasamy, R. Thermal conductivity of unidirectional fibre composites made from yarns and computation of thermal conductivity of yarns. *Indian Journal of Fibre & Textile Research* **2002**, *27*, 217–223.

(S28) Candadai, A. A.; Nadler, E. J.; Burke, J. S.; Weibel, J. A.; Marconnet, A. M. Thermal and mechanical characterization of high performance polymer fabrics for applications in wearable devices. *Scientific Reports* **2021**, *11*, 8705.

(S29) Rahman, M. A.; Dionne, C. J.; Giri, A. Thermally Conductive Self-Healing Nanoporous Materials Based on Hydrogen-Bonded Organic Frameworks. *Nano Letters* **2022**, *22*, 8534–8540.

(S30) Sezginel, K. B.; Asinger, P. A.; Babaei, H.; Wilmer, C. E. Thermal transport in interpenetrated metal–organic frameworks. *Chemistry of Materials* **2018**, *30*, 2281–2286.

(S31) Giri, A.; Evans, A. M.; Rahman, M. A.; McGaughey, A. J.; Hopkins, P. E. Highly negative poisson's ratio in thermally conductive covalent organic frameworks. *ACS nano* **2022**, *16*, 2843–2851.

(S32) Evans, A. M.; Giri, A.; Sangwan, V. K.; Xun, S.; Bartnof, M.; Torres-Castanedo, C. G.; Balch, H. B.; Rahn, M. S.; Bradshaw, N. P.; Vitaku, E., et al. Thermally conductive ultralow-k dielectric layers based on two-dimensional covalent organic frameworks. *Nature Materials* **2021**, *20*, 1142–1148.

(S33) Plimpton, S. Fast parallel algorithms for short-range molecular dynamics. *Journal of Computational Physics* **1995**, *117*, 1–19.

(S34) Thompson, A. P.; Plimpton, S. J.; Mattson, W. General formulation of pressure and stress tensor for arbitrary many-body interaction potentials under periodic boundary conditions. *The Journal of Chemical Physics* **2009**, *131*, 154107.

(S35) Hoover, W. G. Canonical dynamics: Equilibrium phase-space distributions. *Physical Review A* **1985**, *31*, 1695.

(S36) Giri, A.; Hopkins, P. E. Heat transfer mechanisms and tunable thermal conductivity anisotropy in two-dimensional covalent organic frameworks with adsorbed gases. *Nano Letters* **2021**, *21*, 6188–6193.

(S37) Rahman, M. A.; Dionne, C. J.; Giri, A. Pore Size Dictates Anisotropic Thermal Conductivity of Two-Dimensional Covalent Organic Frameworks with Adsorbed Gases. *ACS Applied Materials & Interfaces* **2022**, *14*, 21687–21695.

(S38) Rahman, M. A.; Thakur, S.; Hopkins, P. E.; Giri, A. Engineering the Electronic and Thermal

Properties of Two-Dimensional Covalent Organic Frameworks. *The Journal of Physical Chemistry C* **2023**, *127*, 11157–11166.

(S39) Xu, Y.; Wang, X.; Zhou, J.; Song, B.; Jiang, Z.; Lee, E. M.; Huberman, S.; Gleason, K. K.; Chen, G. Molecular engineered conjugated polymer with high thermal conductivity. *Science Advances* **2018**, *4*, eaar3031.

(S40) Kim, T. W.; Jun, S.; Ha, Y.; Yadav, R. K.; Kumar, A.; Yoo, C.-Y.; Oh, I.; Lim, H.-K.; Shin, J. W.; Ryoo, R., et al. Ultrafast charge transfer coupled with lattice phonons in two-dimensional covalent organic frameworks. *Nature Communications* **2019**, *10*, 1873.

(S41) Chen, X.; Wang, Y.; Wang, J.; Liu, J.; Sun, S.; Zhu, L.; Ma, Q.; Zhu, N.; Wang, X.; Chen, J., et al. A COF-like conductive conjugated microporous poly (aniline) serving as a current collector modifier for high-performance Li–S batteries. *Journal of Materials Chemistry A* **2022**, *10*, 1359–1368.

(S42) Ma, H.; O'Donnel, E.; Tian, Z. Tunable thermal conductivity of π-conjugated two-dimensional polymers. *Nanoscale* **2018**, *10*, 13924–13929.

(S43) Schelling, P. K.; Phillpot, S. R.; Keblinski, P. Comparison of atomic-level simulation methods for computing thermal conductivity. *Physical Review B* **2002**, *65*, 144306.

(S44) Sellan, D. P.; Landry, E. S.; Turney, J.; McGaughey, A. J.; Amon, C. H. Size effects in molecular dynamics thermal conductivity predictions. *Physical Review B* **2010**, *81*, 214305.